Petroleum Science 23 (2026) 5593–5609

Contents lists available at ScienceDirect

Petroleum Science

journal homepage: www.keaipublishing.com/en/journals/petroleum-science

Original Paper

Competitive fracture propagation in Da'an deep shale: A study based on multi-adjacent well collaborative distributed optical fiber monitoring

Jin-Yang Xie [a], Bing Hou [a,b,c,*], Yong-Chun Wu [d], Le He [d], Ju-Hui Zhu [d], Wei Gong [d], Cai-Bao Wang [e]

[a] National Key Laboratory of Petroleum Resources and Engineering, China University of Petroleum, Beijing, 102249, China
[b] Xinjiang Key Laboratory of Intelligent Exploration and Development of Oil and Gas, China University of Petroleum-Beijing at Karamay, Karamay, 834000, Xinjiang, China
[c] College of Petroleum Engineering, China University of Petroleum-Beijing at Karamay, Karamay, 834000, Xinjiang, China
[d] Downhole Services Company, CNPC Chuanqing Drilling Engineering Company Limited, Chengdu, 610051, Sichuan, China
[e] Sinopec Shanghai Offshore Oil & Gas Company, Pudong, Shanghai, 200120, China

ARTICLE INFO

Article history:
Received 9 May 2025
Received in revised form
23 December 2025
Accepted 29 April 2026
Available online 6 May 2026

Edited by Jia-Jia Fei

Keywords:
Distributed optical fiber monitoring
Multi-cluster fracturing
Competitive fracture propagation
True tri-axial hydraulic fracturing
Da'an deep shale gas

ABSTRACT

The competitive propagation of hydraulic fractures during multi-cluster stimulations poses a critical challenge to achieving effective reservoir stimulation in deep shale formations. To address this, our study integrates true triaxial physical simulations with an innovative multi-adjacent well collaborative distributed fiber-optic monitoring strategy. Applied to the deep Longmaxi shale, this approach facilitates full three-dimensional, dynamic tracking of strain evolution, thereby elucidating the mechanisms that govern fracture competition under in-situ stress conditions. The results delineate two distinct fracture architectures dictated by the prevailing stress regime. When the maximum horizontal stress dominates, a cross-shaped network of orthogonal transverse and bedding fractures develops. Conversely, under vertical stress dominance, the combined effects of stress shadowing and geological discontinuities promote the formation of step-like main fractures alongside backward-extending inclined branches. The synchronized interpretation of distributed strain-rate signals—characterized by distinctive patterns such as asymmetric heart-shaped and V-shaped fingerprints—and pump pressure curves elucidates the dynamic process of cluster interaction. This transforms fiber-optic sensing from a monitoring tool into a quantitative diagnostic platform for competitive fracturing. The findings establish a theoretical foundation for designing three-dimensional monitoring frameworks, optimizing cluster spacing, and enabling adaptive pumping strategies, directly supporting the efficient development of deep shale gas resources.

1. Introduction

Against the backdrop of the global transition towards a low-carbon energy structure, shale gas has emerged as a critical, clean, unconventional resource and a pillar of the world's energy strategy. The Longmaxi Formation shale gas system in the Sichuan Basin demonstrates superior resource endowment, having facilitated the establishment of multiple large-scale shale gas fields, including Fuling, Changning, and Luzhou, within the basin and its periphery (Ma and Xie, 2018; Lei et al., 2022; Hou et al., 2022a, 2022b). As a pivotal target for China's shale gas reserve expansion and production growth, the deep Longmaxi Formation shale gas reservoir in the Da'an Block of western Chongqing lies along the southeastern margin of the Sichuan Basin. This reservoir is characterized as a deep marine organic-rich shale, with vertical depths ranging from 3676 to 4454 m. The high-temperature and high-pressure conditions result in significant stress confinement, posing unique challenges for hydraulic fracturing operations (Liang et al., 2024). In

* Corresponding author.
E-mail address: binghou@cup.edu.cn (B. Hou).
Peer review under the responsibility of China University of Petroleum (Beijing).

https://doi.org/10.1016/j.petsci.2026.04.053

contrast to North American shale gas reservoirs, the Longmaxi Formation is characterized by higher organic matter abundance, lower porosity, and a greater content of brittle minerals (Fig. 1). As exploration targets extend into deep complex structural zones, the dynamic competitive propagation of fractures during multi-cluster fracturing demonstrates co-evolutionary control by geological conditions and engineering parameters. This interaction results in complex fracture morphologies, pronounced network heterogeneity, poor connectivity with high-quality reservoir zones, and considerable variability in well productivity (Zou et al., 2021; Zhang et al., 2024).

The competing propagation behavior of multiple fracture systems during shale gas reservoir hydraulic fracturing constitutes a fundamental scientific challenge in determining the effectiveness of reservoir volume stimulation. Current research has been extensively focused on the dynamic competition between intra-cluster fractures, whose evolutionary mechanisms are governed by the coupled effects of geomechanical constraints and engineering parameters (Guo et al., 2021; Tang et al., 2023; Hou et al., 2022a, 2022b). Cluster spacing stands as a critical operational parameter in hydraulic fracturing design. From the perspective of uniform fluid intake, excessively dense arrangements of perforation clusters may restrict fracture propagation within specific clusters under pronounced stress shadowing, where the mutual interference between adjacent fractures significantly alters local stress fields and fluid energy allocation (Hu et al., 2025). Lv and Hou (2024) employ cohesive zone modeling to study multi-cluster fracturing in laminated Lianggaoshan shale. Results show reduced cluster spacing enhances fracture penetration but lowers lamina activation. Optimizing pump rate and cluster spacing improves stimulation efficacy, balancing interlayer plasticity and interface strength constraints. The multi-cluster fracturing process in shale reservoirs exhibits a two-stage fracture propagation dynamic: An initial competitive stage characterized by asymmetric fracture initiation and fluid energy redistribution, followed by a continuous stage dominated by stress shadowing-driven fracture length extension. This competitive behavior intensifies with higher cluster density (Chang et al., 2022). However, this macro-scale competition is fundamentally coupled with multi-scale geological heterogeneities, creating a more complex propagation landscape than previously described. Recent advances reveal that the ultimate fracture network morphology is governed by the interplay between in-situ stress and the topology of pre-existing discontinuities. At a macro-scale, natural fracture networks dictate intersection patterns and connectivity, critically influencing whether hydraulic fractures form productive or less effective intersections (Wang et al., 2025a; Adrian et al., 2025). Simultaneously, at meso-to micro-scales, features such as bedding planes and granular inclusions exert a dominant local control, promoting fracture deflection and branching and enhancing network complexity in a manner sensitive to interfacial properties and approach angles (Wang et al., 2025b, 2025c). This multiscale coupling poses a significant diagnostic challenge, as conventional pressure-transient analysis alone often fails to provide unambiguous insights into fracture closure and competitive dynamics (Ye and Ghassemi, 2024). Consequently, a critical knowledge gap persists in quantitatively understanding the synergistic competition among inter-cluster stress shadows, multi-scale geological heterogeneities, and stress-dependent fracture behaviors under

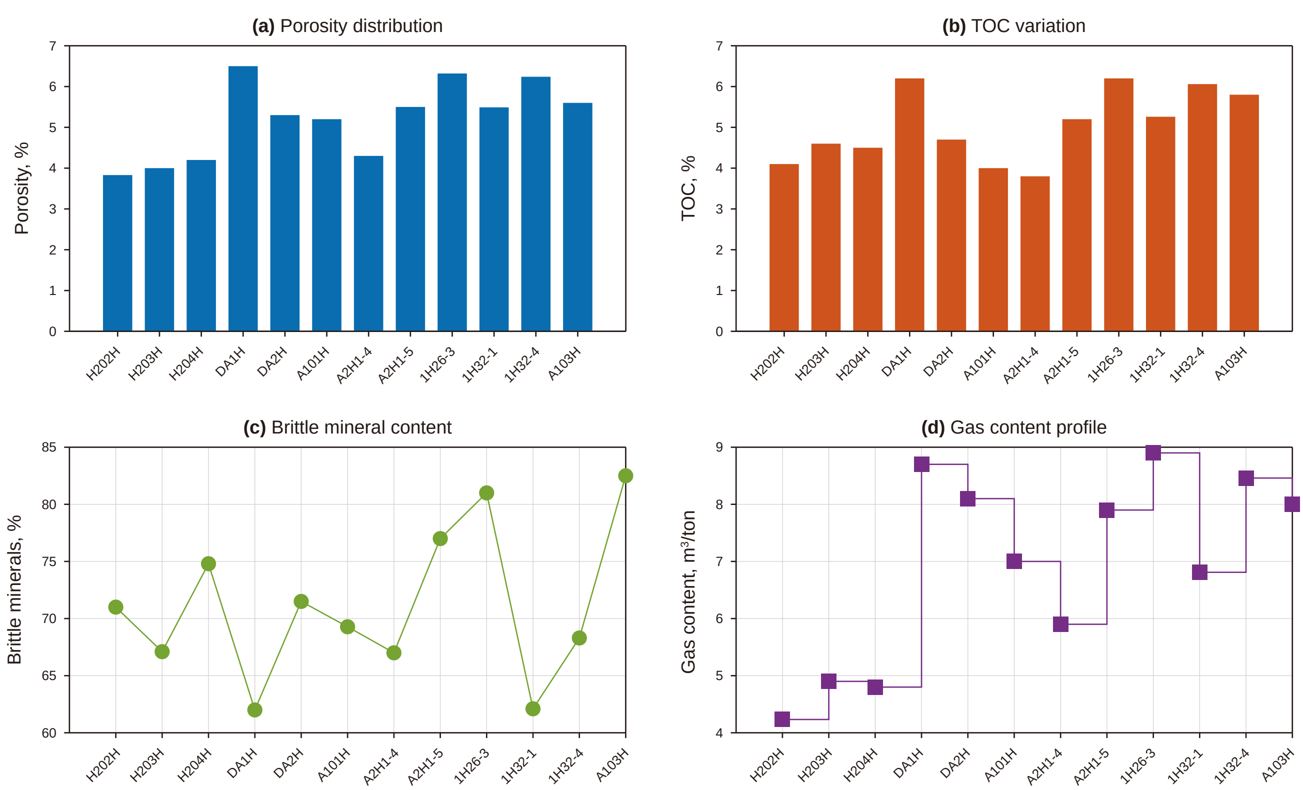

Fig. 1. Basic geological parameters of each well in Da'an Block. (**a**) The porosity distribution of each well in Da'an Block is 4.3%–6.5%, and the whole has the characteristics of low porosity. Hydraulic fracturing is required to obtain industrial gas flow. (**b**) The total organic carbon (TOC) variation of each well in Da'an Block is 3.8%–6.2%, which belongs to the main source rock level and is the main target interval for shale gas development. (**c**) The brittleness content of each well in Da'an block is 62.1%–82.5%, which has the characteristics of high brittleness mineral content and is suitable for hydraulic fracturing. (**d**) The gas content of each well in Da'an Block is 4.2–8.9 m^3/ton. From the perspective of reservoir evaluation, it belongs to a good reservoir and has the value of hydraulic fracturing development.

true three-dimensional in-situ stress conditions—a scenario emblematic of deep shale reservoirs like the Da'an Block.

To capture the full-field strain evolution arising from these intricate multi-scale interactions, distributed optical fiber sensing (DOFS) has emerged as a pivotal technology (Rodriguez and Wuestefeld, 2020). Unlike unsupervised machine learning approaches that excel at tracking slowly evolving fracture properties from seismic data (Nolte et al., 2025) but are less suited for capturing the rapid, highly heterogeneous strain dynamics and asymmetric propagation patterns characteristic of competitive multi-cluster fracturing in deep shale, DOFS provides direct, high-resolution strain measurements. This capability makes it uniquely suited to resolve these complex, transient interactions—driven by stress shadows, bedding planes, and natural fractures. Based on the principles and application scenarios of distributed optical fiber sensing, the technology can be categorized into three main types: distributed acoustic sensing (DAS), distributed temperature sensing (DTS), and distributed strain sensing (DSS) (Sui et al., 2023; Chen et al., 2022). DAS utilizes fiber-optic cables to monitor hydraulic fracturing by analyzing strain responses to fluid-induced acoustic signals (Tan et al., 2021). DAS, first trialed in a 2009 tight-gas well completion, uses telecom-grade fiber-optics to convert backscattered light into acoustic event detections via advanced signal processing. This technology enables real-time hydraulic fracturing monitoring, optimizes design, reduces completion costs, and enhances well productivity and recovery through improved in-wellbore diagnostics (Molenaar et al., 2012). Pakhotina et al. (2020) convert raw DAS data into energy-attribute distributions, enabling quantitative flow-rate estimation per perforation cluster through depth-windowing and fluid-dynamic correlations. Validation against DTS confirms the method's reliability and provides insights into cluster efficiency for multistage treatments. Cramer et al. (2020) evaluate plug-and-perforate designs in shale horizontal wells using multi-diagnostic integration. Staggered perforation patterns with gradual cluster transitions and balanced perforation counts enhanced slurry allocation uniformity, as validated by fracture simulations demonstrating improved cluster efficiency through controlled perforation friction management. DSS technology, based on Rayleigh scattering spectral frequency shifts sensitive to strain/temperature, enables continuous strain monitoring during well shut-in/reopening. DSS-detected extensional strain changes near perforation clusters reveal near-wellbore fracture aperture variations and cluster efficiency, thereby enhancing hydraulic fracture characterization in unconventional reservoirs (Jin et al., 2021). Li et al. (2024) propose a 3D displacement discontinuity method correlating heart-shaped strain signals with hydraulic fracture tip-to-monitor well distances. Modeling reveals linear relationships that enable real-time fracture characterization, validated by HFTS-2 field data, supporting well-spacing optimization for integrity monitoring in unconventional/geothermal reservoirs. Ma et al. (2024) utilize RFS-DSS from vertical monitoring wells to determine effective hydraulic fracture height. Coupled fluid-geomechanical modeling and HFTS-2 field validation reveal that strain-derived fracture tips correlate with pressure data, enabling real-time fracture height monitoring for optimized completions.

In addition to numerical simulation (Dai et al., 2024), the laboratory true triaxial hydraulic fracturing physical simulation of shale reservoirs provides an irreplaceable research approach for revealing complex fracture propagation mechanisms by replicating three-dimensional in-situ stress conditions and engineering fracturing parameters. The research outcomes directly guide fracturing parameter optimization and reduce field trial-and-error costs (Hou et al., 2023). The viscosity of the fracturing fluid significantly influences shale fracture propagation. Hydraulic fractures in shale reservoirs exhibit multi-branched and jagged morphologies during initiation. High-viscosity fracturing fluid reduces the geometric complexity of shale fractures while enhancing their propagation potential (He et al., 2022). Hou et al. (2024) utilize laboratory true triaxial fracturing with distributed fiber sensing to reveal asymmetric fracture swarm propagation patterns in laminated shale, systematically classifying nine propagation behaviors and three fracture network morphologies. Wang et al. (2024) integrated OFDR-based distributed fiber sensing with true triaxial fracturing experiments, revealing bedding fracture initiation/propagation in Sichuan shale through wedge-shaped tensile and bilateral compressive strain zones. Numerical modeling validated these features, providing critical insights for field fiber data interpretation.

To overcome the critical challenges of 'obscured fracture competition dynamics and difficulty in fracture morphology characterization' in deep shale reservoirs, this study focuses on the Longmaxi Formation deep shale in the Da'an Block of western Chongqing. Utilizing a true triaxial physical simulation platform, we conducted multi-cluster hydraulic fracturing experiments by reconstructing in-situ stress fields of deep shale formations. The integrated monitoring system, combining multi-well, collaboratively distributed strain-optical fibers, enabled real-time tracking of the full-cycle evolution of the strain field during fracture initiation, deflection, and closure. This research aims to establish a mechanistic understanding of the competitive propagation. We specifically investigate two core theoretical questions: (1) What are the controlling factors that dictate whether multiple fractures propagate sequentially or quasi-simultaneously? (2) How do stress shadow effects and geological discontinuities synergistically govern the ultimate fracture network architecture under different in-situ stress regimes? Addressing these questions provides theoretical underpinnings and technical methodologies for deep shale exploitation, while offering referential guidance for shale gas development in analogous geological settings.

2. Multi-cluster hydraulic fracturing experiment of deep shale monitored by distributed optical fiber

2.1. Experimental materials and experimental equipment

2.1.1. Geological section and outcrop acquisition of Longmaxi Formation

Field investigations indicate that the Long1 Sub-member of the Longmaxi Formation is primarily composed of black carbonaceous shale, siliceous shale, and gray silty shale. These lithologies reflect a depositional environment transitioning from deep-water anoxic conditions to relatively shallower-water settings. This interval is enriched with well-preserved biogenic fossils, including diverse graptolite species (Fig. 2) and siliceous radiolarians, which exhibit exceptional paleontological characteristics critical for stratigraphic subdivision and paleoenvironmental reconstruction. The exceptional preservation of these fossils indicates predominantly anoxic-reducing depositional conditions, which were highly conducive to the preservation and enrichment of organic matter.

Vertical profiling shows a gradual lithological transition from basal dark, organic-rich shales to lighter-colored shales at the top, accompanied by upward-coarsening grain-size trends. This vertical succession reflects a progressive shift from deep-water stagnant phases to relatively shallow or higher-energy depositional regimes. Notably, the sub-member exhibits a remarkably high siliceous content (>65%), derived from dual contributions: siliceous organisms (radiolarians and diatoms) in deep-water environments and hydrothermal silica inputs. Such elevated silica content not only enhances the shale brittleness index but also

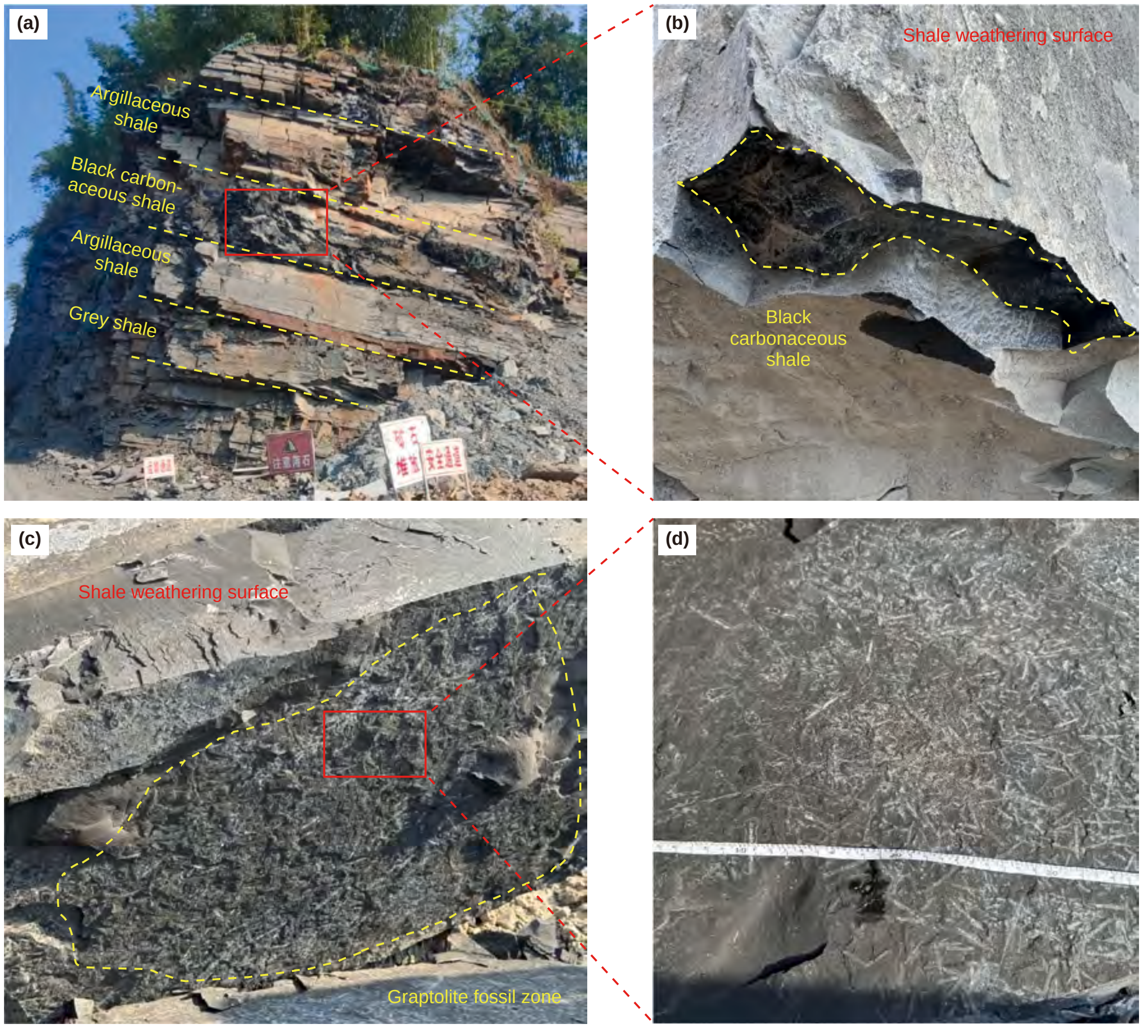

Fig. 2. Shale profile of Longmaxi Formation and weathering surface of black carbonaceous shale. (**a**) Shale profile of Longmaxi Formation. (**b**) Weathering surface of black carbonaceous shale. (**c**) and (**d**) The graptolite fossil zone indicates that the sedimentary environment is deep water. The well-preserved fossils indicate that the environment during the sedimentary period was dominated by anoxic reduction, which is extremely conducive to the preservation and enrichment of organic matter.

creates favorable reservoir conditions through improved pore network connectivity for shale gas storage. Therefore, this paper obtains the outcrop here as an experimental sample. The basic mechanical parameters of shale obtained through triaxial compression tests (confining pressure = 20 MPa) and Brazilian split tests are presented in Table 1.

2.1.2. True triaxial hydraulic fracturing system

To investigate the fracture propagation mechanisms during multi-cluster fracturing in deep shale reservoirs of western Chongqing, we employ a large-scale true triaxial hydraulic fracturing simulation system (Fig. 3). The true triaxial hydraulic fracturing simulation system comprises seven core components: (1) true tri-axial experimental system, (2) MTS servo supercharging system, (3) oil-water separator, (4) hydraulic pressure stabilizer, (5) multi-channel data acquisition platform, and (6) real-time data processing unit, with its schematic configuration illustrated in Fig. 4. The original system has been improved by adding (7) a distributed fiber optic sensing system (details in Section 2.1.3) and (8) an acoustic emission monitoring system. The system enabled real-time tracking of the full-cycle evolution of the strain field during fracture initiation, deflection, and closure.

Table 1
Basic mechanical parameters of the shale sample.

Elastic modulus, GPa	Poisson's ratio	Compressive strength, MPa	Tensile strength, MPa
19.9	0.31	288.2	7.0

To replicate subsurface reservoir conditions, the experimental protocol requires rigorous simulation of in-situ stress fields. For vertical well simulations, two orthogonal pairs of flat jacks (*X-Y* plane) generate horizontal principal stresses (σ_H and σ_h), while the vertical loading assembly applies overburden stress (σ_v) through independent servo-control. In horizontal well configurations, the vertical flat jack system instead applies the minimum horizontal principal stress (σ_H), with the *X-Y* jacks simulating σ_H and $\sigma_{v,}$ respectively. The multi-channel MTS pressure regulation system delivers hydraulically amplified loads (0–70 MPa) through these flat jacks, enabling precise application of true triaxial stress states to the cubic shale specimen (300 × 300 × 300 mm). During stimulation, the MTS servo-pump injects fracturing fluid from a 700 mL pressure vessel (100 MPa) into the wellbore via a dual-

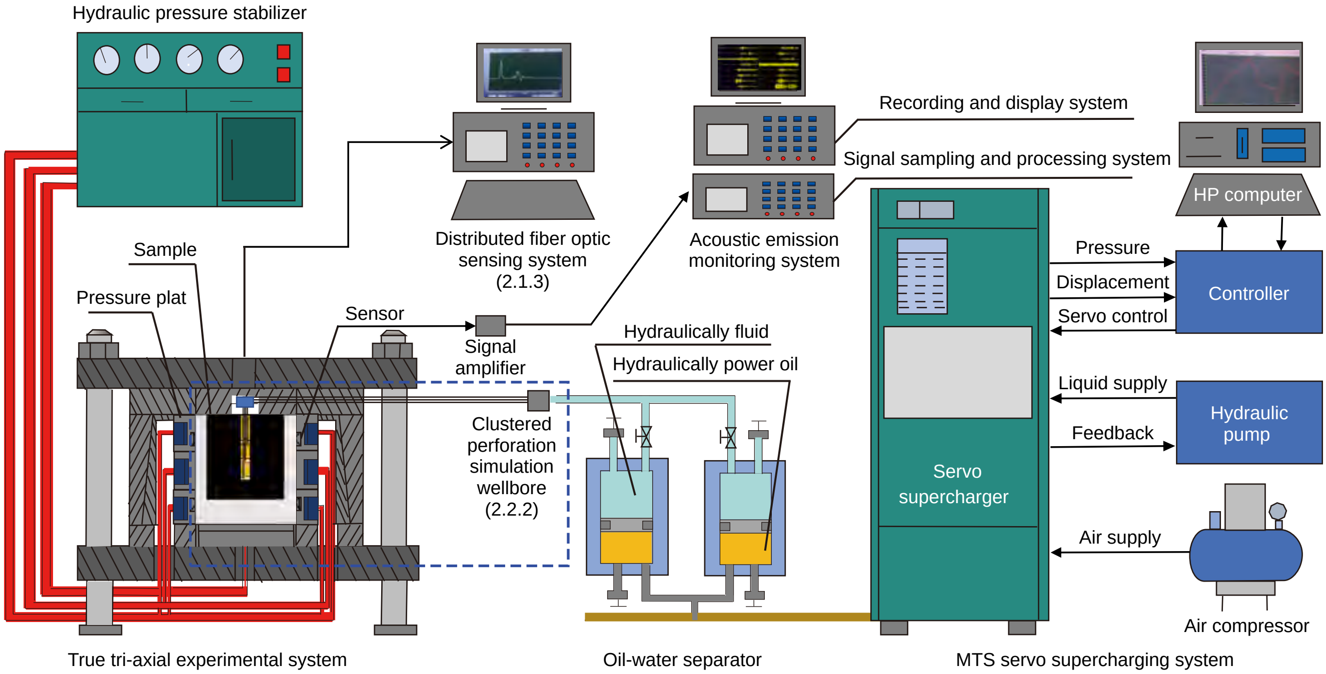

Fig. 3. Improved true tri-axial hydraulic fracturing system. The improved experimental system can simulate multi-cluster hydraulic fracturing in deep shale and monitor the characteristics of fracture initiation and propagation.

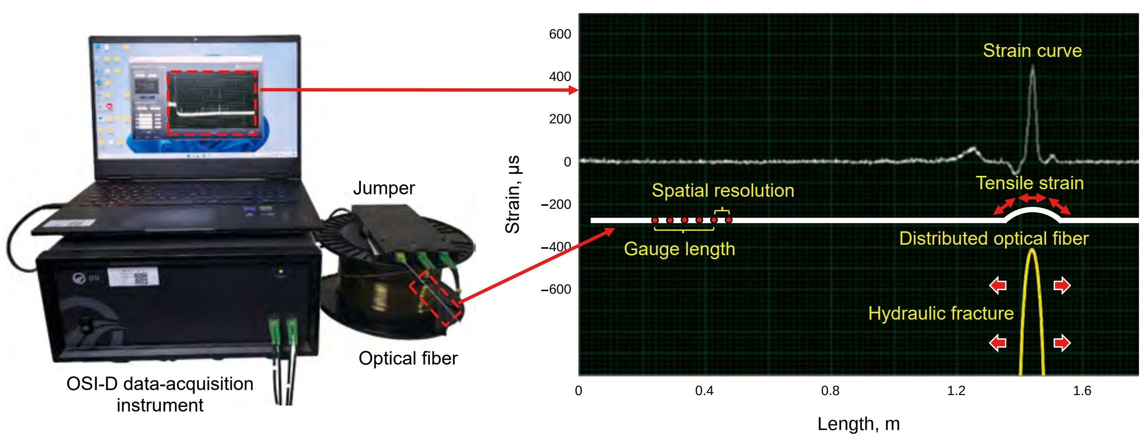

Fig. 4. Distributed fiber optic monitoring equipment and principles. OSI-D high-precision DOFS system under dynamic monitoring of a single hydraulic fracture to the fiber propagation process of the display.

piston displacement mechanism. This novel dual-piston design (2 × 1000 mL) enables alternating fluid injection phases through programmable valve sequencing.

2.1.3. *Distributed fiber optic sensing system*

DSS technology enables monitoring of strain variations in formations during hydraulic fracture propagation. To investigate the dynamic fracture growth in multi-cluster fracturing of deep shale reservoirs in western Chongqing, the experimental setup employs the high-precision OSI-D distributed fiber optic sensing system, primarily composed of the OSI-D data-acquisition instrument, jumper, and auxiliary components (Fig. 4). The OSI-D system demodulates backward Rayleigh scattering signals generated during hydraulic fracturing using OFDR (Chen et al., 2016), thereby tracking temperature and strain changes during fracture propagation. This allows for dynamic inversion of fracture growth processes, facilitating real-time monitoring of fracture initiation and propagation.

$$\frac{\Delta\lambda}{\lambda} = -\frac{\Delta\nu}{\nu} = K_\varepsilon \varepsilon_f + K_T \Delta T \tag{1}$$

where λ is the average optical wavelength; $\Delta\lambda$ is the optical wavelength shift amount; ν is the average optical frequency; $\Delta\nu$ is the frequency shift; K_ε is the strain sensitivity coefficient; ε_f is the fiber strain; K_T is the temperature sensitivity coefficient; ΔT is the temperature variation.

Key monitoring parameters include spatial resolution and gauge length. Spatial resolution is the minimum distance the system can discern, determined by the laser's wavelength-sweep range, since the light's propagation speed in the fiber is constant. Gauge length refers to the distance between paired pulses along the fiber in multi-pulse systems. Their differences are illustrated in Fig. 4, with spatial resolution typically ≤ gauge length.

In hydraulic fracturing experiments, strain responses during fracture initiation and propagation can be monitored in horizontal, vertical, or inclined adjacent wells by adjusting fiber deployment configurations (Liu et al., 2020). This enables comprehensive analysis of dynamic fracture behavior and post-fracture geometry. Strain changes are defined as positive for tensile strain and negative for compressive strain. System parameters include a spatial resolution of 1.28 mm, a gauge length of 10.28 mm, a sampling frequency of 8 Hz, a fiber core diameter of 125 μm, and a strain measurement accuracy of ±1 με.

2.2. Innovative experimental methods

2.2.1. Multi-adjacent well collaborative distributed strain optical fiber wiring method

This study proposes an innovative multi-well, collaborative, distributed optical fiber strain deployment configuration (Fig. 5) that demonstrates substantial technical superiority over conventional U-shaped and unidirectional fiber arrangements for shale reservoir fracturing monitoring. The term "multi-adjacent well collaborative" in this study refers to a distributed fiber-optic deployment strategy designed to simulate multi-well field observation conditions for comprehensive monitoring of three-dimensional fracture propagation during single-well fracturing. By establishing a dual-directional strain field monitoring network—comprising both perpendicular (simulating offset horizontal wells in adjacent layers and vertical observation wells) and parallel (simulating same-layer horizontal offset wells) orientations relative to shale bedding planes—this methodology overcomes the single-parameter monitoring constraints inherent to unidirectional fiber layouts that typically only effectively capture either fracture height or width. The implemented system enables simultaneous acquisition of dynamic evolution parameters for both vertical height propagation in fractures and horizontal width extension.

Comparative analysis of the U-shaped configuration and multi-well collaborative strain-optical fiber deployment reveals inherent trade-offs between monitoring efficacy and operational complexity. The U-shaped layout offers simplified deployment procedures and enhanced fiber survivability, yet is constrained to single-parameter monitoring (fracture height or width) with spatial resolution limitations. In contrast, the multi-well system simultaneously monitors fracture height evolution and width propagation via strain-rate field analysis (Table 2). However, this advanced method imposes stringent experimental requirements.

2.2.2. Clustered perforation simulation wellbore design method

This study designed a clustered perforation simulation wellbore assembly to investigate multi-cluster competitive fracture initiation mechanisms (Fig. 6). A 23 cm × 23 cm × 23 cm shale outcrop was encased within a 30 × 30 × 30 cm concrete mold using high-strength cementitious material (adhesives). The experimental protocol commenced with drilling an 18 cm vertical borehole (*Φ*20 mm) into the shale outcrop. Initial preparation involved injecting a 1 cm-thick sodium chloride particle into the borehole. The first wellbore conduit (*Φ*3 mm) was then precisely positioned within the salt layer to prevent conduit obstruction from grout flowback during cementing operations. High-performance grout was subsequently pumped to a 5 cm fill height using pressure-controlled injection. Following a 72-h curing period under controlled conditions, this process was iteratively repeated with sequential conduit installations at differential depths, achieving multi-cluster zonal isolation through precision cement sheath formation.

2.2.3. Basic experimental process

The methodology encompasses specimen preparation, wellbore simulation, fiber-optic instrumentation, and concrete encapsulation, establishing a controlled analog for in-situ reservoir conditions. Key innovations include the deployment of OSI-D high-resolution sensing systems and clustered perforation wellbores, enabling dynamic strain characterization during fracture network evolution under true 3D stress states (Fig. 7).

(a) The shale outcrop surface is meticulously polished with sandpaper to remove surface impurities, followed by documentation of initial integrity conditions. (b) The outcrop is fully wrapped with cling film and adhesive tape to preserve bedding structures. A vertical counterbore (18 cm depth, 1 cm diameter) is drilled at the

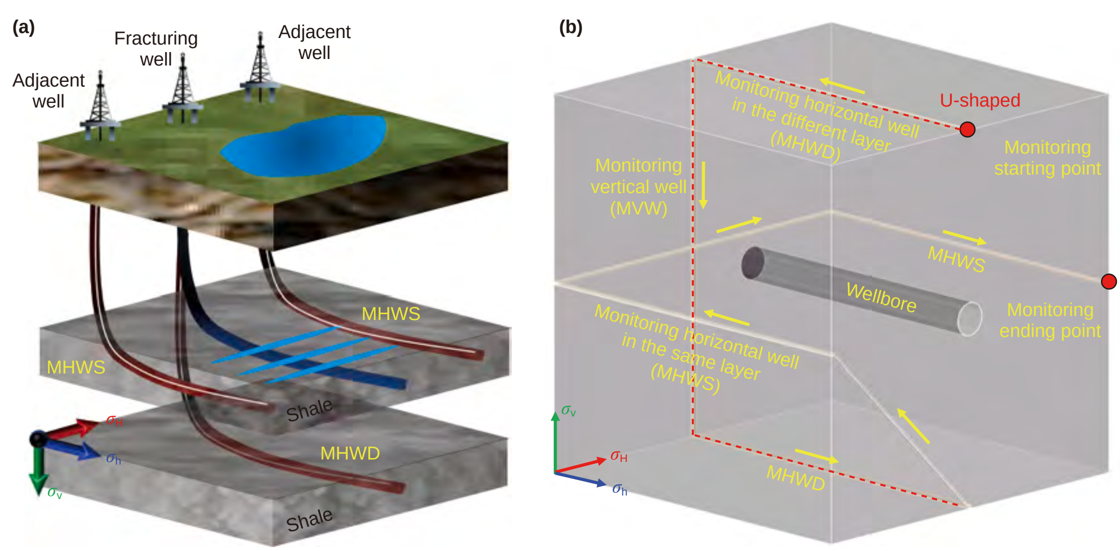

Fig. 5. Multi-adjacent well collaborative distributed strain optical fiber wiring method. (**a**) A conventional on-site well arrangement method (well factory) for monitoring fracturing propagation. The red wellbore represents the adjacent well (monitoring well), the white curve represents the outer fiber, and the blue wellbore represents the fracturing well. (**b**) The gray cube is a rock sample, and the white line on its surface is the optical fiber's layout track. The yellow arrow indicates the distribution order of optical fiber data points. The red dotted line represents the traditional U-shaped method.

Table 2
Comparison of U-shaped and multi-adjacent well method.

Optical fiber layout mode	U-shaped method		Multi-adjacent well method
Characteristics of optical fiber wiring	Vertical to shale bedding	Parallel to shale bedding	Both
Fracture parameter monitoring	Monitoring fracture height	Monitoring fracture width	Monitoring of both

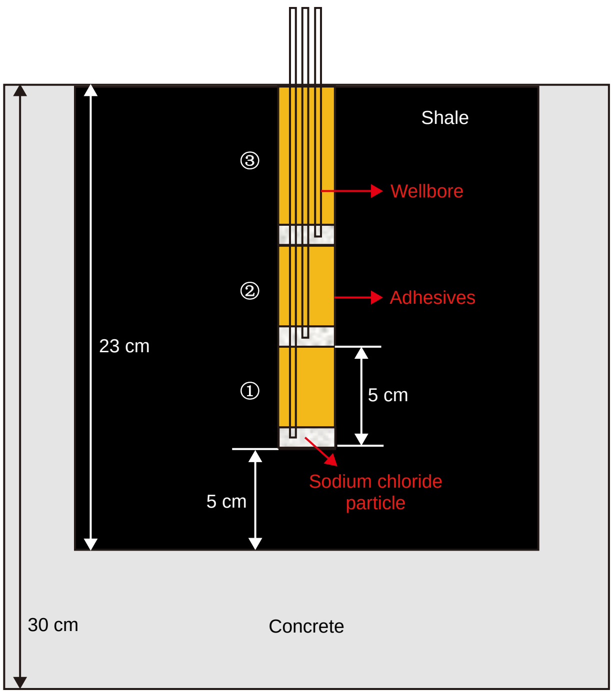

Fig. 6. Clustered perforation simulation wellbore design method. The simulation system incorporates three modular wellbore conduits strategically positioned at varying depths within the specimen through sequential cementing operations. Each conduit is interconnected via four-way valves, enabling flexible injection configurations: simultaneous three-cluster, individual-cluster, or temporary plugging modes.

specimen's center using a drilling rig. (c) A precision mechanical process creates 1 mm-deep linear grooves along predefined paths on the shale surface, serving as fiber-deployment channels. (d) Three clustered perforation simulation wellbores (2 m in length, 3 mm in diameter) are inserted into wellheads at designated depths, with the annular spaces sealed using cementing adhesive. (e) Pretreated optical fibers are embedded into the grooves, using a specialized adhesive to achieve fiber-shale coupling. (f) The instrumented shale outcrop is precisely positioned at the center of a 30 × 30 × 30 cm cubic mold. (g) A 7 cm elevated spacer is placed at the mold base prior to concrete pouring. Vibration compaction densifies the material, followed by surface finishing after curing. (h) The prepared specimen is mounted in a true triaxial loading system to conduct hydraulic fracturing simulations while dynamically monitoring strain responses.

3. Competitive expansion mechanism of multi-cluster fracturing in deep shale

3.1. Multi-cluster fracturing experimental scheme of Da'an block

In true triaxial hydraulic fracturing experiments, laboratory-scale stress configurations must replicate the in-situ stress regime of shale formations with the highest possible fidelity. Utilizing dimensional analysis principles and field-derived geomechanical data from oil reservoir stress profiling, experimental parameters were derived using similitude scaling relationships, as detailed in Table 3 (Hou et al., 2014; Xie et al., 2024). It is essential to account for pore pressure by subtracting it from the total stress to maintain consistency between the laboratory-derived effective stress and the field confining pressure calculated via the similarity criterion.

In the deep shale formations of western Chongqing Block, the in-situ stress regime predominantly exhibits $\sigma_H > \sigma_V > \sigma_h$. Based on this geomechanical configuration, Experiment 1# was designed with maximum horizontal stress as the principal loading condition. However, multi-phase tectonic activity has developed normal fault systems in the study area, formed by crustal extension under vertical tensile stress. Such structural units maintain $\sigma_V > \sigma_H > \sigma_h$ stress relationships, which critically influence the propagation behavior of hydraulic fracturing. To comprehensively evaluate the impact of principal stress variations on fracture geometry, Experiment 2# was concurrently conducted with overburden pressure as the dominant stress component.

3.2. Under the condition of horizontal maximum stress as the dominant condition

The post-fracturing morphology displays distinct characteristics, as shown in Fig. 8(a). Following the initiation of the first cluster, a vertical main fracture propagates longitudinally. The fracture initiation direction is perpendicular to the wellbore and bedding direction, which is a transverse fracture. Concurrently developed horizontal bedding fractures intersect orthogonally with vertical transverse fractures, forming a cross-shaped fracture pattern. Notably, while surface observation suggests fracture deflection at bedding-plane intersections (Fig. 8(a)), detailed fracture-face analysis in Fig. 9(a) reveals no fracturing-fluid imbibition traces in these transitional zones. These non-conductive segments are therefore classified as dry fractures, demarcated by yellow dashed lines in Fig. 8(c).

The 3D propagation pattern of the initial cross-cutting fracture cluster is explicitly illustrated in Fig. 9(a). Initiated from the near-wellbore zone of the first perforation clusters, the fracture demonstrates pronounced unilateral asymmetric propagation. The fracture plane exhibits hydraulic energy anisotropy dissipation during extension. Stress barrier analysis reveals that the horizontal stress difference dominantly constrains vertical fracture growth. After penetration through bedding interfaces, the fracture tip blunts. According to the minimum energy principle in fracture mechanics, the fracture tip is ultimately captured by the bedding-plane fracture system, forming a characteristic stress barrier termination. Fig. 9(b) delineates the bedding-plane fracture propagation with characteristic bilateral differential extension. Post-capture by bedding weak planes, the vertical transverse fracture triggers shear activation mechanisms. The activated multi-thin bedding fractures exhibit asymmetric unilateral propagation and an under-expanded area.

3.2.1. Analysis of monitoring results

The integrated analysis method, which combines distributed fiber-optic monitoring with laboratory-true triaxial hydraulic fracturing pressure curves, enables dynamic interpretation of

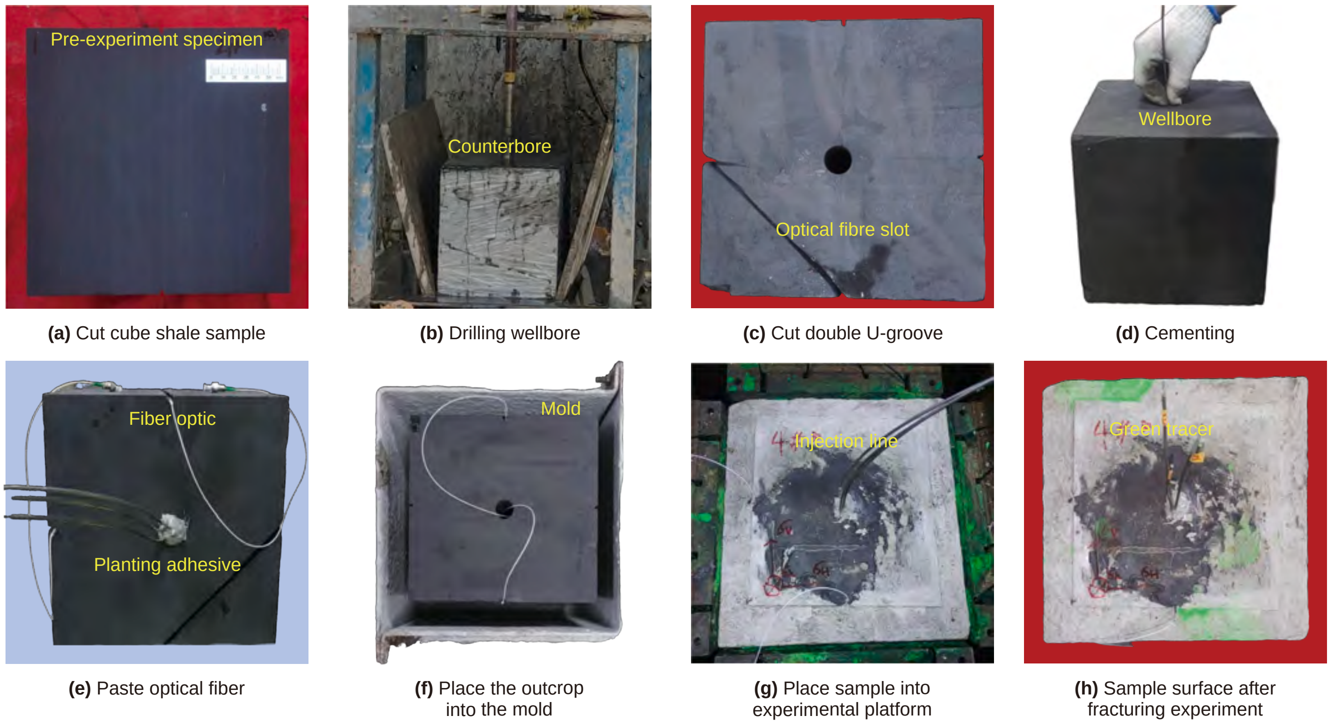

Fig. 7. Experimental process for multi-adjacent well collaborative distributed optical fiber monitoring technology with true triaxial physical simulations.

Table 3
Experimental scheme.

Sample number	In-situ stress $\sigma_v/\sigma_H/\sigma_h$, MPa		Pump rate, m^3/min		Viscosity, mPa·s	
	Lab	Field	Lab	Field	Lab	Field
1	23/25/10	103/105/90	6×10^{-5}	18	10	20
2	25/23/10	105/103/90	6×10^{-5}	18	10	20

hydraulic fracture propagation processes. Distributed fiber-optic sensing, through continuous strain-rate waterfall maps covering the rock surface, reveals heterogeneous strain accumulation near the advancing fracture tip. Millisecond-level synchronization between these strain rate maps and critical inflection points in the pressure curve (fracture pressure peaks, propagation pressure fluctuations) has significantly enhanced the accuracy of fracture initiation timing determination.

(1) Analysis of pump pressure curve

Based on the characteristic analysis of pumping pressure curves derived from conventional hydraulic fracturing experiments, the fracture propagation process can be categorized into four distinct phases (Fig. 10):

a. Initial pressure buildup phase. This phase corresponds to fluid filling during initial injection, characterized by a monotonic pressure increase that is proportional to the volume of fracturing fluid injected.
b. Near-wellbore fracture initiation phase. Upon reaching critical breakdown pressure, tensile failure occurs in rock formations, generating initial fractures near the wellbore. This process manifests as the first pressure peak followed by an abrupt pressure decline at Point B.
c. Cross-lamination fracture propagation phase. This stage exhibits pronounced pressure oscillations (sawtooth-shaped fluctuations), with dynamic mechanisms intrinsically linked to periodic hydraulic fracture penetration through bedding planes. Specifically, when fracture fronts encounter bedding interfaces, additional energy is required to overcome the interfacial cementation strength, leading to localized pressure surges. Subsequent bedding plane penetration enables rapid fracture extension along low-resistance paths, triggering pressure drops. This alternating process of stress barrier breakthrough and fracture path redirection constitutes characteristic pressure responses in heterogeneous bedding formations.
d. Boundary-constrained propagation phase. As fracture fronts approach specimen boundaries, fluid loss induces a rapid decline in inlet pressure until dynamic equilibrium is established between fluid loss and injection rates. This signifies the complete development of fracture network conductivity and the experimental termination.

(2) Analysis of distributed optical fiber strain rate waterfall diagram

Asymmetric propagation mechanism of cognate transverse fractures. Zones ① and ③ manifest as a single transverse through-going fracture on the specimen surface (Fig. 9(a)). Distributed optical fiber monitoring reveals a symmetric spatial distribution of strain rate signals between the two zones. However, the average strain rate amplitude in Zone ③ is 70% lower than that in Zone ①, indicating restricted fracture propagation in Zone ③ and confirming Zone ① as the dominant fluid pathway. Post-fracturing core sectioning confirmed a significantly higher abundance of retained fracturing fluid in Zone ① compared to Zone ③ (Fig. 9(a)). This asymmetric propagation is mechanistically attributed to stress redistribution at the fracture tip when it intersects bedding

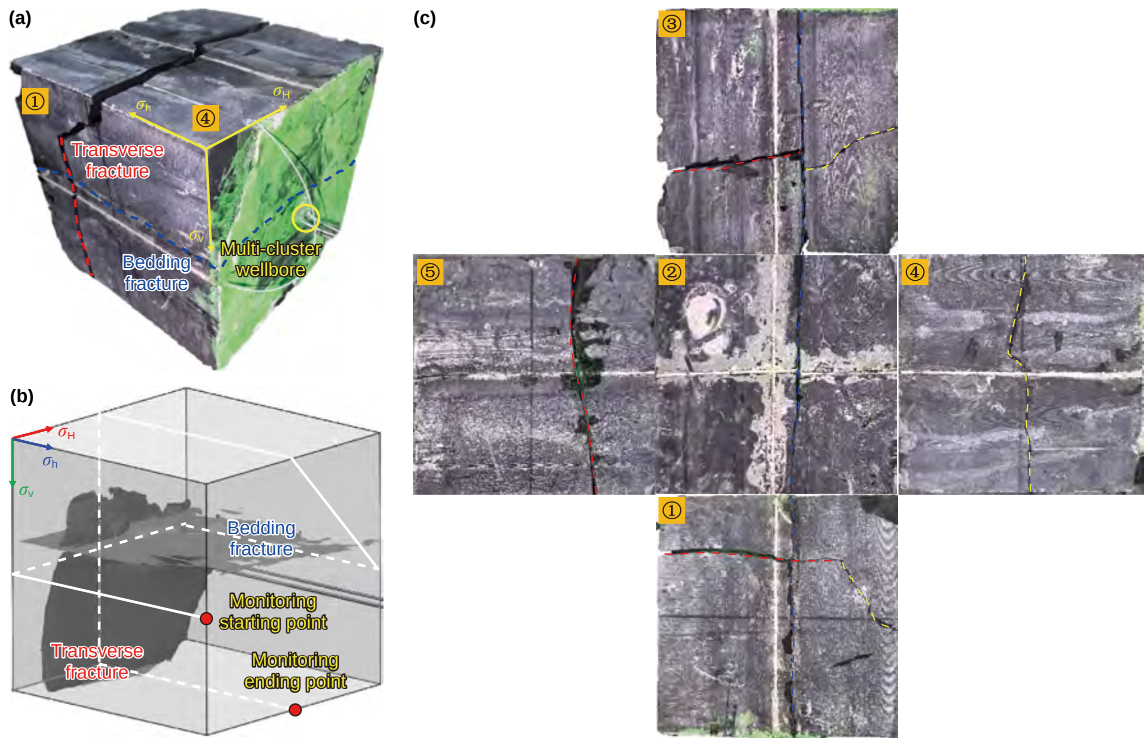

Fig. 8. The fracture morphology and reconstruction of sample No. 1 after hydraulic fracturing experiment. (**a**) Rock samples after the hydraulic fracturing experiment. (**b**) 3D scanning fracture surface reconstruction diagram. The white line in the image is the optical fiber wrapped on the surface of the rock sample. (**c**) Plane expansion diagram of each surface of the rock sample after pressing. The red dotted line represents the transverse fracture. The blue dotted line represents the bedding fracture. The yellow dotted line represents the dry fracture, which was not affected by fracturing fluid.

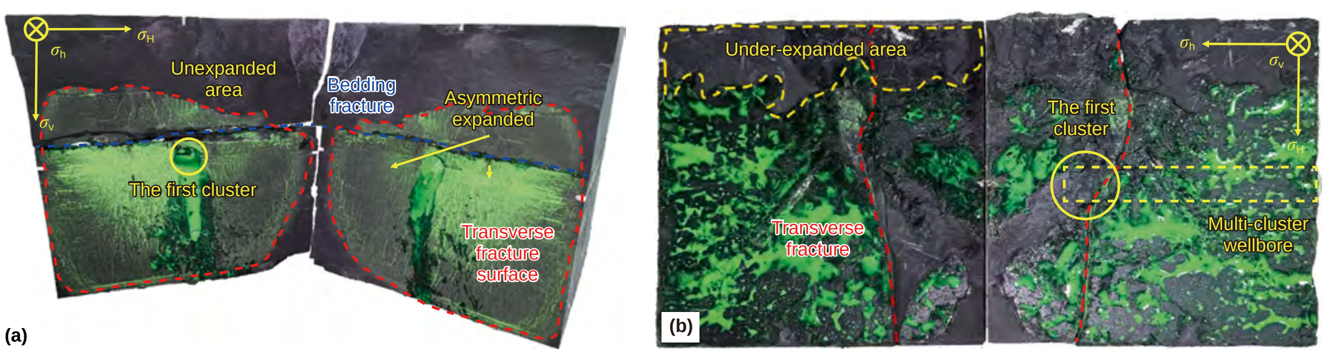

Fig. 9. The fracture surface diagram of sample No. 1 after hydraulic fracturing experiment. (**a**) Transverse fracture surface expansion diagram. The area delineated by the red dashed line represents the fracturing fluid coverage zone, which corresponds to the actual fracture surface. The blue dotted line represents the bedding fracture. (**b**) Bedding fracture surface expansion diagram. The red dotted line represents the transverse fracture.

planes (discontinuous interfaces), where interfacial properties induce heterogeneous stress-field evolution.

Fracture shadow response and fracture height containment mechanism. Distributed strain rate monitoring in Zone ④ detected no significant signal response (threshold <10 με/s), indicating that hydraulic fractures failed to propagate effectively into this region. Post-fracturing core verification revealed a height-restricted non-propagated zone influenced by bedding fractures, where fracture vertical growth was mechanically arrested.

V-shaped strain response and bedding-plane competition mechanism. Distributed strain rate signals in Zone ② exhibit a distinctive V-shaped distribution (Fig. 9(b)), reflecting the competitive capture of fluid energy between two adjacent bedding-plane weaknesses. The peak strain rate at the upper bedding interface exceeds that at the lower interface by 92% at $t=$ 605, ultimately forming a single dominant flow channel through mechanical selectivity. Post-fracturing core sectioning confirms incompletely propagated zones along the bedding fracture surfaces. This selective activation is a direct manifestation of how local heterogeneity of bedding plane dictates the redistribution of limited fluid energy under a uniform remote stress, leading to a single dominant flow channel.

Asymmetric heart-shaped strain response and fracture deflection mechanism. The strain rate in Zone ⑤ exhibits an asymmetric heart-shaped distribution, with the fracture preferentially extending toward the heel-end side (larger response region), where the heart-shaped apex aligns with the fracture initiation point. Three-dimensional fracture reconstruction confirms that the competitive dominance between overburden stress and maximum horizontal principal stress ($\Delta=$ 2 MPa) governs the oblique propagation trajectory. The small stress difference creates a near-isotropic horizontal stress state near the fracture tip,

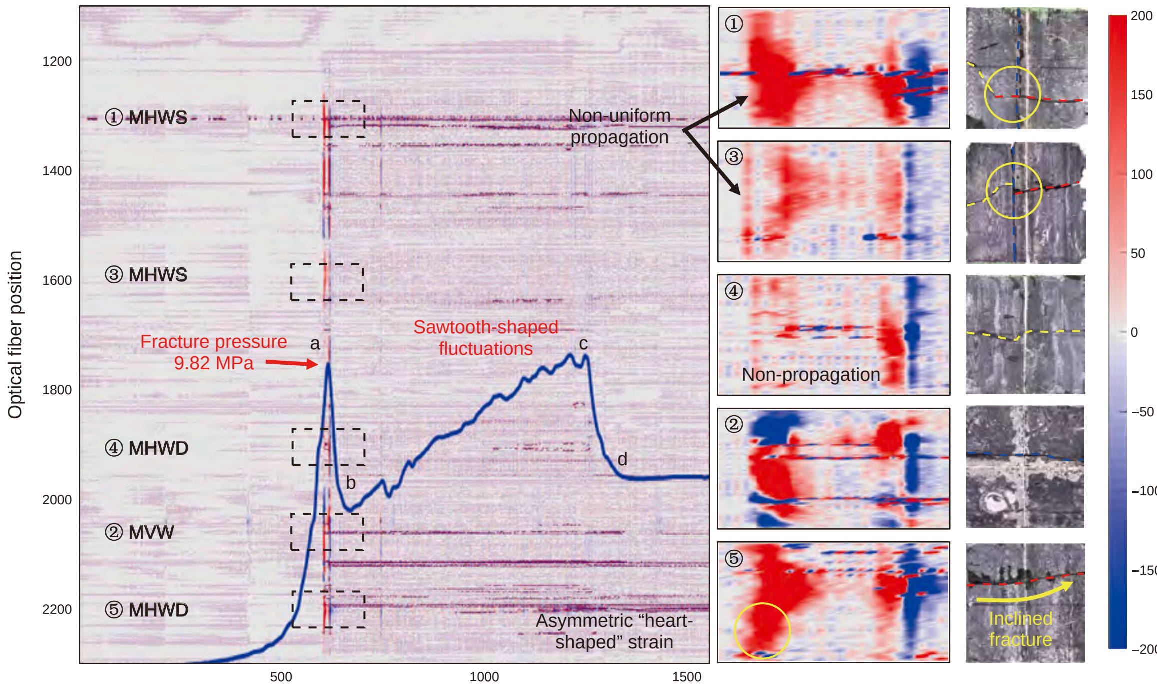

Fig. 10. The waterfall diagram interpreted jointly by the pump pressure curve of sample No. 1 and the distributed optical fiber strain rate. The red dotted line on the view of each surface of the rock sample represents the transverse fracture, and the blue dotted line represents the bedding fracture. The yellow dotted line represents the dry fracture, which is not affected by fracturing fluid. The enlarged numbered strain-rate waterfall on the right corresponds to the black-dotted rectangular area on the left. The analysis mode matches the monitoring effect with the actual rock sample after the actual experiment.

diminishing the directional guidance of the far-field stress. In this scenario, the fracture path becomes highly susceptible to local perturbations, such as those induced by the growing fracture itself or minor heterogeneities, leading to the observed deflection. This illustrates how reduced stress anisotropy can promote complex, non-planar fracture competition.

3.2.2. Mechanistic interpretation of fracture propagation under σ_H-dominance

The fracture behaviors observed under σ_H-dominance, including asymmetric cross-shaped networks and characteristic strain signals, are governed by the interplay of fracture mechanics principles and geological heterogeneity. The initial transverse fracture propagation perpendicular to bedding is dictated by the maximum tensile stress criterion, following the direction normal to the minimum horizontal stress (σ_h). When this fracture interacts with a bedding plane, a mixed-mode (I + II) fracture tip process ensues. The significantly lower tensile strength of the bedding interface leads to a local redistribution of the stress intensity factors, resulting in a marked increase in the Mode-II (shear) component (K_{II}). This promotes shear activation and slip along the bedding, forming orthogonal branches. The V-shaped strain signal (Fig. 10, Zone ②) quantitatively reflects the competitive shear failure between adjacent bedding planes, with the higher strain-rate peak indicating the dominant capture path. The heart-shaped strain pattern (Zone ⑤) and associated fracture deflection are direct evidence of stable fracture kinking under a perturbed local stress field, consistent with predictions from the maximum circumferential stress criterion.

3.3. Under the condition of vertical stress as the dominant condition

The post-fracturing fracture propagation characteristics of the specimen are shown in Fig. 11, revealing a complex fracture network formed by multi-cluster synergistic propagation. Controlled by the coupled effects of vertical geostress differences, bedding-plane weakness, natural fractures, and inter-cluster interference, the fracture morphology exhibits significant differentiation and complexity. Cluster 1 develops a vertical stepped main fracture, while Cluster 3 forms an inclined transverse fracture, with their propagation paths showing a back-to-back distribution. The fracture system is dominated by transverse fractures, locally superimposed with bedding-induced stepped branches and stress-interference-driven deflected fractures. Notably, the semi-wing asymmetric extension of Cluster 3 highlights the regulatory effects of heterogeneous distribution of formation pressure and inter-cluster stress shadowing on fracture morphology.

The fractures initiated in Cluster 1 develop into a typical stepped transverse fracture (Fig. 11(c)), with an evolutionary process divided into three phases: During the initial fracturing stage, the fracture initiates strictly perpendicular to the wellbore axis and bedding planes, following the orientation control of the maximum principal stress (overburden pressure), and vertically extends from the perforation to form a continuous transverse fracture body (corresponding to the bottom section of the stepped fracture surface). In the bedding activation stage, as the fracture propagates to bedding plane weaknesses, these weak planes are activated, inducing localized deflection (see the central deflection segment in Fig. 11). Driven by the vertical stress difference, the fracture penetrates the bedding. It resumes vertical extension, forming the upper transverse fracture. The final morphology exhibits a composite stepped structure, with the bottom and upper transverse fractures connected by bedding deflection segments, resulting in an alternating "vertical-bedding-vertical" propagation pattern. Discontinuous growth paths caused by bedding weaknesses result in a stepped geometric configuration.

Under the coupled effects of vertical geostress difference and stress shadowing from Cluster 1, the propagation of Cluster 3 fractures is significantly modulated. The net pressure generated by

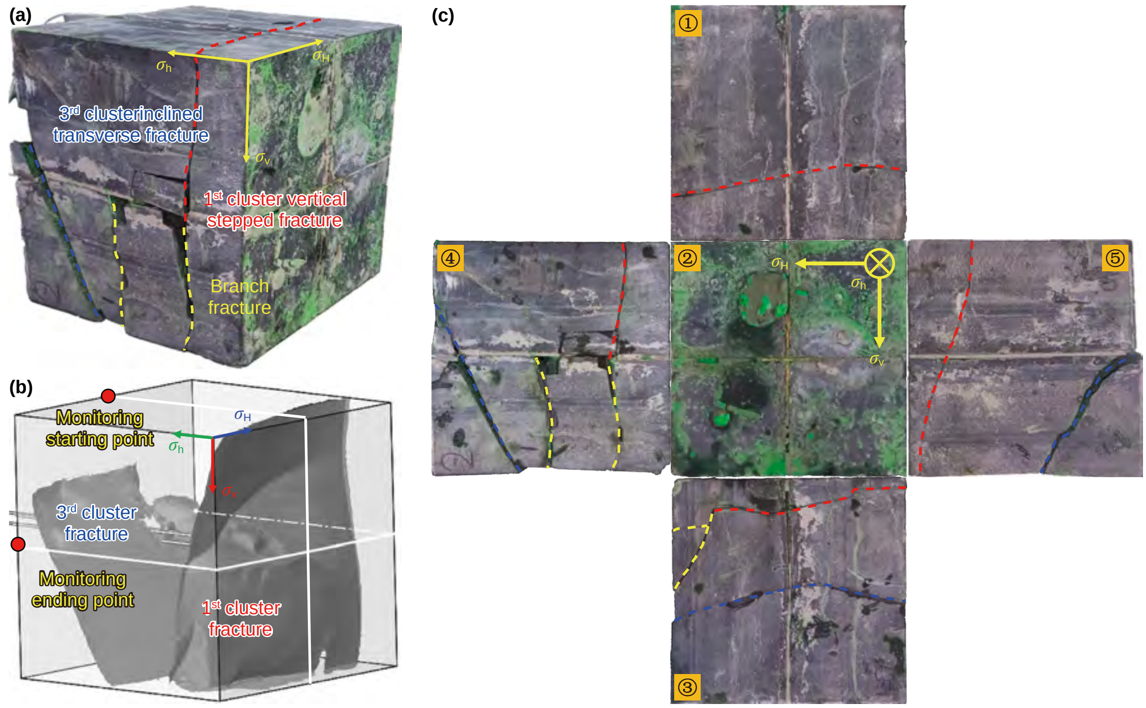

Fig. 11. The fracture morphology and reconstruction of sample No. 2 after hydraulic fracturing experiment. (**a**) Rock samples after the hydraulic fracturing experiment. (**b**) 3D scanning fracture surface reconstruction diagram. The white line in the image is the optical fiber wrapped on the surface of the rock sample. (**c**) Plane expansion diagram of each surface of the rock sample after pressing. The red dotted line represents the 1st cluster stepped fracture. The blue dotted line represents the 3rd cluster inclined transverse fracture. The yellow dotted line represents the branch fracture.

Cluster 1 fractures reshapes the local stress field, causing deflection of the maximum horizontal principal stress direction. Within this altered stress field, fractures in Cluster 3 are forced to propagate backward relative to Cluster 1 at the transverse plane boundary, forming an inclined transverse main fracture. The backward-extending branches further interact with bedding planes, developing reverse-stepped fractures. The final composite morphology of “inclined transverse fracture + reverse-stepped fracture” (Fig. 12) is established, with the deflection angle (30°) quantitatively reflecting the intensity of inter-cluster interference.

3.3.1. Analysis of monitoring results

(1) Analysis of the pump pressure curve

Due to the highly complex fracture network geometry in Sample #2, the corresponding pump pressure curve exhibits significant heterogeneity. Conventional fracturing curve analysis (Fig. 13) is limited to a preliminary three-stage classification of the propagation process and fails to resolve key mechanisms effectively.

PC 1 segment: Initiation and propagation of single-cluster dominant fracture. The inlet pressure increases linearly with continuous fracturing fluid injection, forming localized high pressure near the wellbore. When the pressure reaches the critical breakdown pressure (16.3 MPa), the stress-concentrated zone around the perforation cluster first attains the rock tensile strength, leading to fracture initiation. The dominant cluster preferentially opens, followed by a sharp pressure drop post-fracture initiation.

PC 2 segment: Sequential fracture initiation under stress shadowing. The multiple minor pressure rebounds indicate that subsequent clusters initiate not simultaneously, but sequentially. This is a direct consequence of stress shadowing: the net pressure from the first dominant fracture (C1) has locally increased the minimum principal stress in the vicinity of neighboring clusters. Therefore, clusters like C3 must build up significantly higher wellbore pressure (up to 22.5 MPa) to overcome this superimposed stress and initiate, resulting in the observed delayed and high-pressure initiation events. This segment vividly captures the transition from a single dominant fracture to a suppressed, competitive initiation phase.

PC 3 segment: Vertically heterogeneity-driven stepwise fracture propagation. When vertical fracture growth encounters shale bedding planes, pressure spikes are required to breach these layers, reflecting bedding-controlled vertical fracture extension. Consequently, the pressure curve exhibits periodic step-like fluctuations, with fractures deflecting along weak bedding planes to form a step-like fracture network.

(2) Analysis of distributed optical fiber strain rate waterfall diagram

The heterogeneous pressure responses caused by the asymmetric propagation of multiple-cluster fractures, interference from bedding planes/natural fractures, and superimposed stress shadows make it challenging to distinguish fracture initiation sequences solely from a single pressure curve. However, distributed optical fiber monitoring can effectively identify the initiation, propagation, and interaction of fractures in such heterogeneous reservoirs.

Due to the reliance of multi-cluster fracture initiation analysis on “spatial resolution capabilities”, this experiment employed strain waterfall plots to highlight the spatial competition relationships among multi-cluster fractures.

DSS1 phase (main fracture initiation). At $t=$ 1.8 min, the first cluster of fractures initiated bidirectionally along the specimen's

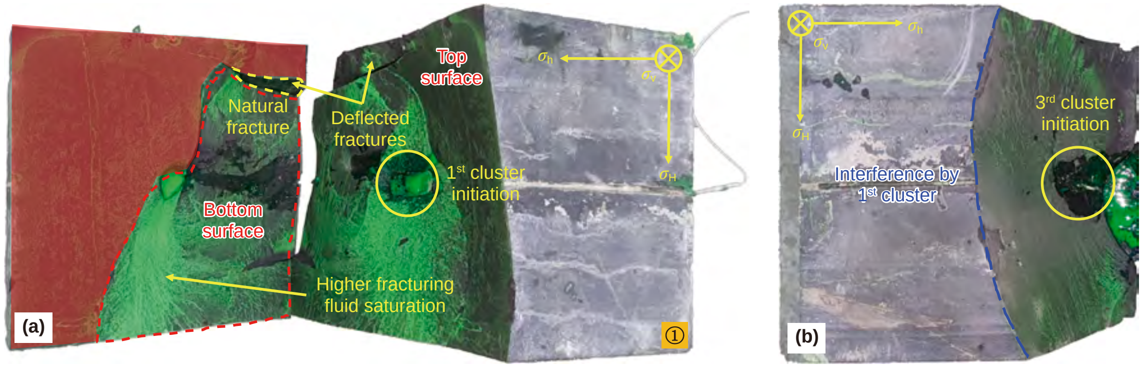

Fig. 12. The fracture surface diagram of sample No. 2 after hydraulic fracturing experiment. (**a**) The 1st cluster stepped fracture surface. Affected by natural fractures, the fracture surface is divided into the top surface (red transparent surface) and the bottom surface (red dotted line frame surface). (**b**) The 3rd cluster is an inclined transverse fracture. The red dotted line represents the 1st cluster stepped fracture surface.

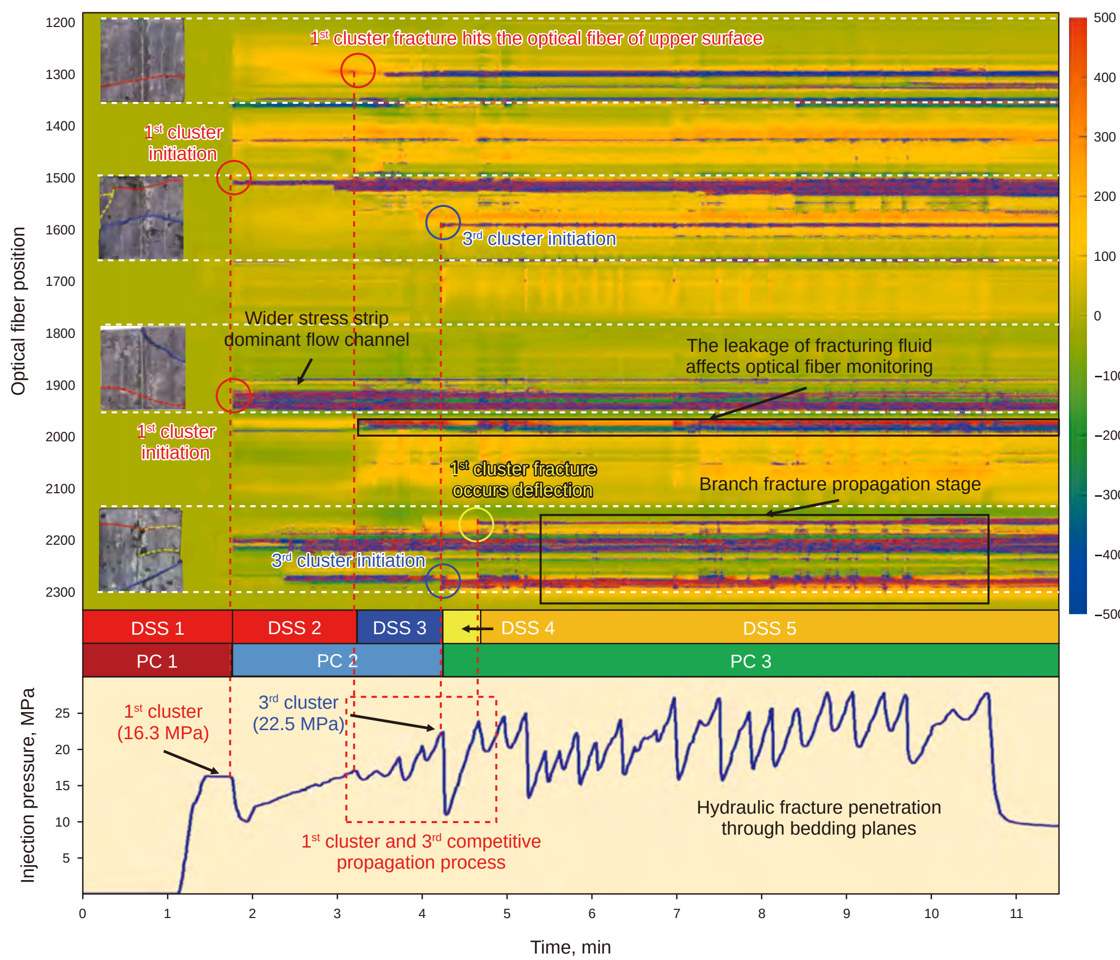

Fig. 13. The waterfall diagram interpreted jointly by the pump pressure curve of sample No. 2 and the distributed optical fiber strain rate. The red circle represents the first cluster of fracture, the blue circle represents the second cluster of fracture, and the yellow circle represents the first cluster of branch fracture. DSS represents a stage-criterion method based on the optical fiber strain signal, and PC represents a stage-criterion method based on the pump pressure curve. They have different resolutions for fracture initiation, propagation, and interaction, and optical fibers can monitor more detailed fracture evolution processes.

bottom surface (3) and side surface (5) (Fig. 13). The strain waterfall plot revealed that the strain response bandwidth on the side surface (5) (ΔW= 51.2 mm) was significantly larger than that on the bottom surface (3) (ΔW= 12.8 mm), indicating the formation of a dominant flow conduit along the maximum horizontal principal stress direction (side surface 5). The "strain response bandwidth" (ΔW) refers to the spatial extent along the optical fiber, measured in millimeters (mm), over which a significant strain signal is detected during a fracturing event. Post-fracturing observations validated this conclusion: the side surface (5) exhibited significantly higher fracturing fluid saturation than the bottom surface (3), consistent with the spatial distribution of strain signals.

DSS2 phase (bedding constraint effect). At t= 3.1 min, the main fracture propagated vertically to the top boundary (1), triggering a characteristic strain reversal ($\Delta\varepsilon$ abruptly shifted from +412 to −500 με). Comprehensive analysis suggests that while fracturing fluid preferentially accumulated along the side surface (aligned with the maximum horizontal stress), the earlier arrival of the fracture at the top boundary (1) implies that vertical penetration through bedding layers remains more challenging than horizontal propagation, even when the overburden stress exceeds the maximum horizontal stress. Notably, the pump pressure curve at t= 2.1 min displayed a "sharp rise followed by gradual decline", indicating hydraulic connectivity between the main fracture and natural fractures, which induced deflection of the propagation path.

DSS3 phase (cluster interference effect). After the third cluster initiated at t= 4.2 min, fracturing fluid redistribution occurred: the newly opened flow channel at the top surface (1) reduced fluid intake at the side surface (5) and increased intake at the bottom surface (3). Following a brief stabilization, repressurization at 4.2 min triggered a clear response, confirming the initiation of the third cluster and its propagation toward the side surface (4) and the bottom surface (3). The weak tensile strain on the side surface (5) and the absence of synchronous signals on the top surface (1) suggested that the new fracture exhibited an inclined single-wing propagation pattern. This phenomenon demonstrates that the stress shadow effect not only delays initiation but also actively steers the propagation path of subsequent fractures. Unable to extend symmetrically towards the high-stress shadow region created by C1, the C3 fracture is mechanically diverted, resulting in the observed inclined, single-wing (back-to-back) propagation pattern. This is a clear example of how stress shadows dictate not just "if" but "how" a competing fracture grows.

DSS4 phase (branch fracture activation). At t= 4.7 min, a new strain peak ($\Delta\varepsilon$= 293 με) emerged on the side surface (4), accompanied by declining flow in the original fracture clusters, confirming a dynamic alternating propagation mechanism in the multi-cluster system. Abnormal fluctuations in the pump pressure curve during this phase exhibited strict spatiotemporal correlation with fiber-optic-monitored fracture competition events, highlighting the unique advantages of distributed fiber sensing in diagnosing complex fracture networks.

DSS5 phase (dominant channel migration). After t= 4.7 min, strain responses at monitoring points became concentrated on the bottom (3) and side (4) surfaces, indicating competition between branch and deflected fractures. During t= 5.5–7.0 min, branch fractures and deflected fractures exhibited intense competition: Initially, fracturing fluid preferentially flowed along deflected fractures. However, as branch fractures breached bedding interfaces (strain bandwidth surged by ΔW= 5.1 mm at t= 7.0 min), the tortuosity of branch fractures (τ= 1.08) became 10% lower than that of deflected fractures (τ= 1.20). According to the principle of hydraulic energy minimization (preferential flow through low-resistance paths), the dominant flow channel shifted from deflected to branch fractures. This transition manifests in strain signals as widening branch fracture strain bands and narrowing deflected fracture bands. This dynamic shifting of the dominant flow pathway between competing branches is a real-time manifestation of the principle of hydraulic energy minimization. The fracture network self-organizes by continuously selecting the lowest-resistance path, leading to a non-uniform, time-dependent fluid distribution among multiple fractures that characterizes complex, competitive propagation.

3.3.2. Mechanistic interpretation of fracture propagation under σ_V-dominance

The complex "step-like" and "back-to-back" fracture patterns under σ_V-dominance arise from a tripartite mechanical coupling: stress shadowing, bedding plane activation, and multi-cluster competition. The step-like geometry of the main fracture is a signature of sequential fracture capture and re-initiation across bedding planes. The vertical fracture, upon encountering a bedding interface, branches horizontally due to the lower energy required for interface shear slip (Mode-II dominance) compared to tensile penetration. Subsequent re-initiation of a vertical fracture above the bedding results from the restored dominance of the far-field σ_V over σ_h, completing one "step". This process repeats, creating a composite fracture path. The backward propagation and inclination of the third cluster fracture are unambiguous consequences of local stress field rotation induced by the stress shadow of the first cluster. This altered stress trajectory forces the new fracture to seek a path of maximum energy release away from the compressive shadow zone. The real-time migration of the dominant flow channel, diagnosed by DSS, exemplifies fluid–solid coupling and path-dependent competition. The lower-tortuosity branch fracture eventually becomes favored due to reduced hydrodynamic impedance, demonstrating how fluid flow selectivity can dynamically overprint the initial stress-controlled fracture architecture.

4. Discussion of mechanistic insights into competitive fracture propagation and applications

4.1. Mechanisms and implications of competitive fracture growth

4.1.1. Controlling factors for sequential vs. quasi-simultaneous growth

Our experimental results, interpreted through the lens of fracture mechanics, allow us to delineate the controlling factors governing the competition between multiple clusters of fractures. The transition from simultaneous initiation to sequential propagation is primarily determined by the dynamic interplay between fluid energy allocation and mechanical interference (Fig. 14).

Factor 1: Stress shadow intensity and superposition. This is the paramount factor suppressing simultaneous growth. As soon as a fracture initiates, it creates a localized zone of increased compressive stress perpendicular to its face. For a subsequent cluster to initiate and propagate within this stress shadow, the net pressure must overcome not only the virgin rock strength but also this additional stress increment. Our DSS data (the absence of strong signals in certain zones in Figs. 10 and 13) provides direct evidence of this suppression. When clusters are closely spaced, their stress shadows can superimpose, creating a stress barrier that can completely prevent the initiation of middle clusters, leading to a strictly sequential mode.

Factor 2: Near-wellbore friction and perforation efficiency. Before any fracture extends far, competition within the wellbore occurs. Uniform fluid entry across all perforations is ideal for simultaneous initiation. However, inherent minor differences in perforation quality or the use of limited-entry designs can create variable perforation friction. This leads to preferential fluid intake into the cluster with the lowest resistance, granting it a 'first-mover advantage' and triggering a sequential chain reaction.

Factor 3: In-situ stress anisotropy and geological heterogeneities. As shown by the contrast between Experiments 1# and 2#, the far-field stress regime sets the stage. A large horizontal stress difference strongly confines fractures to a planar geometry, making competition primarily a race for length within a single plane, often won by a

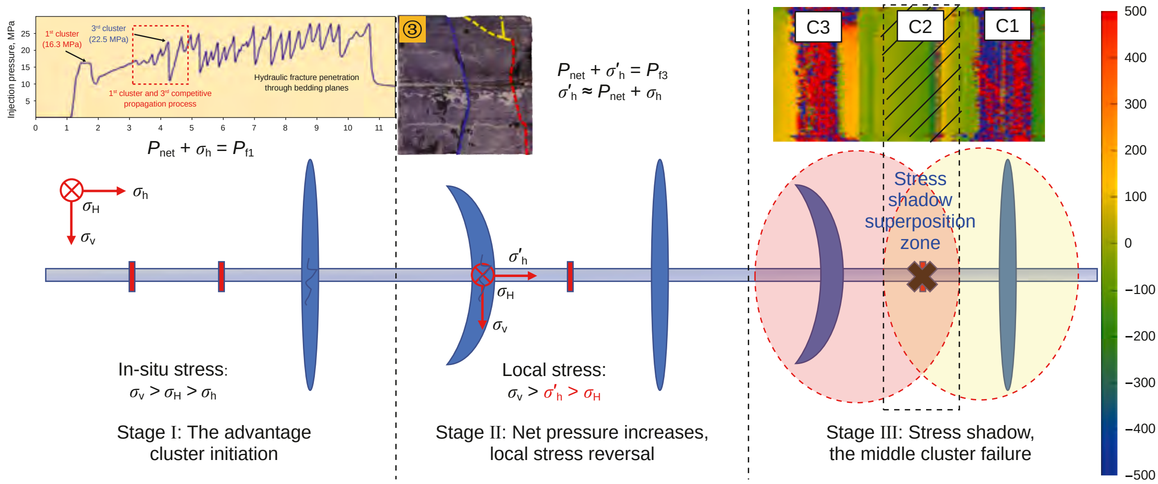

Fig. 14. The dominant role of the stress shadow superposition zone and fracture competition mechanism. The competitive propagation of multi-cluster fractures is divided into three stages: The advantage cluster initiation, net pressure increases-local stress reversal, and stress shadow superposition-the middle cluster failure.

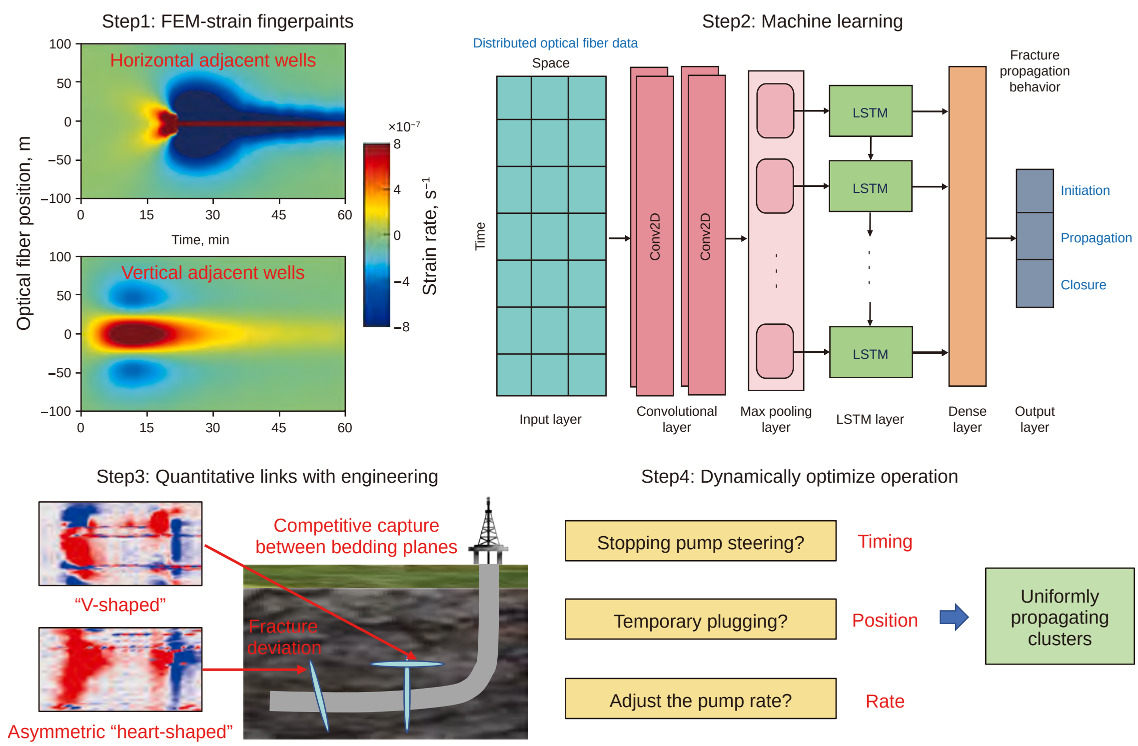

Fig. 15. An intelligent fracturing optimization framework integrating distributed optical fiber sensing and machine learning.

single cluster. Conversely, a lower stress anisotropy or the presence of abundant bedding planes/natural fractures provides escape paths. Later-activated clusters, though suppressed in the primary direction, can be captured by these weaknesses (Fig. 12), leading to a more complex, quasi-simultaneous activation of multiple, geometrically distinct fracture branches.

Integrating the above factors, we propose a generalized, three-stage evolution model for multi-cluster competition in deep shale (Fig. 14):

Stage I: Preferential initiation & dominant channel formation: Driven by Factor 2 and often the toe-side end effect, 1–2 clusters initiate first, establishing dominant flow channels.

Stage II: Stress shadow establishment & local stress reversal: The dominant fractures extend, their stress shadows intensify (Factor 1), and begin to alter the local principal stress orientations around adjacent clusters.

Stage III: Adaptive competitive growth: Subsequent clusters initiate under this altered stress field. Their propagation paths are no longer determined solely by the far-field stress. Still, they are a compromise between the far-field stress, the local stress shadow (Factor 1), and the available geological weaknesses (Factor 3). This results in deflected, inclined, or backward-growing fractures (as seen in Cluster 3 of Experiment 2#), completing the complex fracture network.

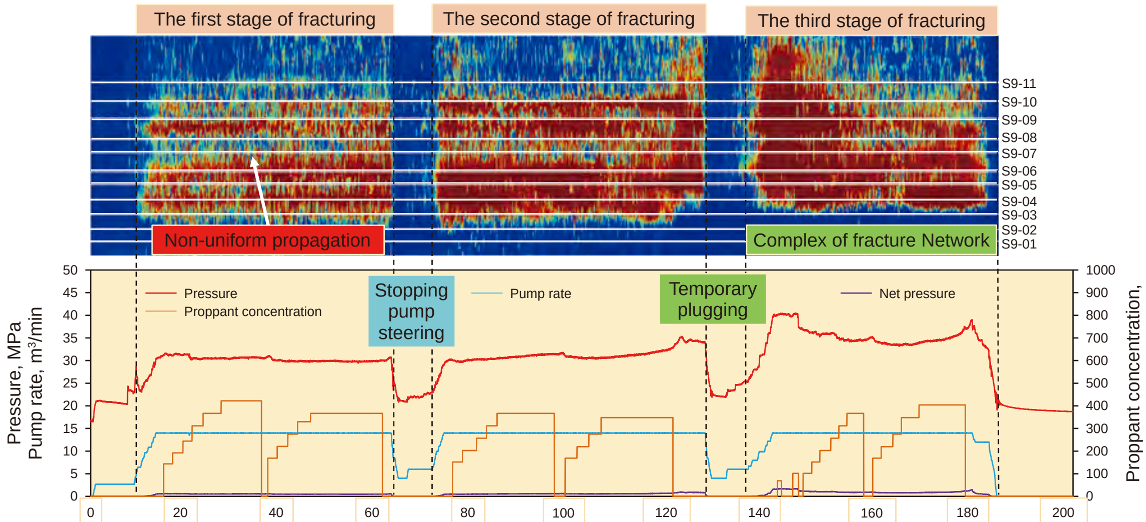

Fig. 16. Optical fiber signal and fracturing operation curve of the 9th segment of Well YS-A. The synchronous analysis method for distributed optical fiber and pump pressure curves is applied at the oilfield site, accurately monitoring uneven liquid inflow caused by inter-cluster interference and adopting measures such as stopping pump steering and temporary plugging to increase the complexity of the fracture network effectively.

4.1.2. Distributed optical fiber sensing: from phenomenological monitoring to quantitative diagnosis

DOFS has evolved from a simple data-recording tool into a powerful platform for the quantitative diagnosis of subsurface fractures. This study establishes direct correlations between strain-rate signal characteristics and fracture-propagation mechanisms, providing the basis for a fiber-based diagnostic toolkit for competitive fracturing.

Synchronizing DSS with pump pressure resolves ambiguities in pressure analysis alone, and the high-resolution OSI-D system enables the creation of a strain fingerprint library. For example, an asymmetric heart-shaped pattern indicates fracture deflection, while a V-shaped signal reveals competitive capture between bedding planes. The strain response bandwidth (ΔW) further approximates the fracture's influence range, quantitatively confirming features like dominant flow pathways. Looking forward, the next step is to establish quantitative links between strain fingerprints and engineering outcomes. With machine learning, real-time DSS data could dynamically optimize pumping parameters, shifting from static pre-job design to a cognitive, adaptive process (Fig. 15).

4.2. Applications of the integrated interpretation of distributed fiber-optic data and pump pressure curves in the field

During multi-cluster fracturing operations in horizontal wells, fluctuations in treating pressure are influenced by fracture propagation patterns and proppant transport behavior. Events such as intersections with natural fractures/bedding planes, abrupt increases in fracture height, length restrictions, or proppant bridging can be reflected in pressure signatures. However, the ambiguity in pressure response complicates downhole diagnostics. DOFS reveals a correlation between treating pressure evolution and active cluster count. Field implementation was conducted at Well YS-A in the Da'an Block, Sichuan Basin, using a multi-cluster competition model and integrated fiber-optic pressure diagnostic technology (Fig. 16).

Well YS-A targets the Longmaxi Formation (lateral length: 1195.4 m; TVD: 1140–1450 m) with average reservoir properties of 4.3% porosity, 3.5% total organic carbon, and 3.5 m^3/t gas content. The 1165.5-m stimulated interval was divided into 13 stages with 125 clusters (90–100 m/stage, 6–9 m cluster spacing). Each stage employed 9–11 clusters (10.5-mm perforations at 0.32–0.38 m^3/min/perf) using slick water (3–5 mPa·s viscosity) and 70/140-mesh + 40/70-mesh sand (proppant intensity: 2.5–3.0 t/m; fluid intensity: 22–26 m^3/m). Limited-entry perforation and plug-and-perf techniques were applied to enhance cluster efficiency. In Stage 9 (96 m, 11 clusters at 6–9 m spacing), Clusters 1–2 showed no fluid intake. Initial asymmetric fracture growth was observed: During phase 2, a 3.0-MPa pressure rise (1.4 MPa net pressure increase) triggered Cluster 11 activation, consistent with lab-observed toe-side cluster prioritization and mid-cluster stress shadowing. Post-diversion with 75 kg diverters induced a 6.6-MPa pressure surge (2.6 MPa net pressure gain) in phase 3, activating mid-clusters and reducing stage heterogeneity by 12%. Fiber data validated the positive correlation between pressure increments and diversion effectiveness.

Lab-field bidirectional validation was achieved: True triaxial experiments accurately predicted cluster activation sequences, diversion thresholds, and fracture orientation in Well YS-A. Conversely, fiber-pressure integrated analysis optimized cluster efficiency, fracture prediction, and diversion timing, significantly improving fracture network complexity and stimulated reservoir volume.

5. Conclusions

This study establishes an innovative framework for monitoring competitive fracture propagation in deep shale reservoirs by integrating multi-adjacent well collaborative distributed fiber sensing with true triaxial physical simulations. By overcoming the critical limitations of conventional monitoring techniques in resolving complex fracture networks, we systematically reveal the following key conclusions:

(1) The proposed multi-adjacent well collaborative distributed strain optical fiber wiring method simulating adjacent horizontal and vertical monitoring wells achieves comprehensive dynamic tracking of both vertical and horizontal propagation of fractures. This technology accurately identifies non-conductive fracture branches, providing direct

technical support for optimizing perforation cluster placement and fluid allocation in field-scale shale development.

(2) Synchronized analysis of distributed fiber-optic strain signals and pump pressure curves precisely delineates the temporal-spatial sequence of multi-cluster fracture initiation and the dynamic mechanisms of cluster interference. The tripartite coupling of stress shadow intensity, near-wellbore fluid allocation efficiency, and in-situ geological heterogeneities governs the transition from sequential to quasi-simultaneous growth. Toe-side clusters often gain a preferential initiation advantage. In contrast, heel-side or middle clusters exhibit delayed initiation and deflected (back-to-back) propagation paths under the influence of established stress shadows.

(3) The in-situ stress regime primarily dictates the ultimate fracture network architecture. Under maximum horizontal stress dominance, fractures propagate as orthogonal transverse-laminar hybrid systems. In contrast, vertical stress dominance promotes the development of step-like main fractures alongside reverse-growing inclined branches. Within these stress-defined frameworks, bedding plane weaknesses and pre-existing natural fractures act as critical local modifiers, inducing fracture deflection, branching, and capture, thereby adding significant complexity to the network.

(4) Distributed fiber-optic sensing has evolved from a phenomenological monitoring tool into a quantitative diagnostic platform for competitive fracturing. Characteristic strain-rate fingerprints (V-shaped, heart-shaped) are directly correlated with underlying mechanisms such as bedding plane competition and fracture deflection. This capability, when integrated with pump pressure analysis, enables real-time diagnosis of fracture interactions and inefficient growth zones, paving the way for data-driven adaptive fracturing optimization.

CRediT authorship contribution statement

Jin-Yang Xie: Writing – original draft, Visualization, Validation, Software, Investigation, Formal analysis. **Bing Hou:** Writing – review & editing, Supervision, Resources, Project administration, Methodology, Funding acquisition, Data curation, Conceptualization. **Yong-Chun Wu:** Supervision. **Le He:** Resources. **Ju-Hui Zhu:** Data curation. **Wei Gong:** Validation. **Cai-Bao Wang:** Formal analysis.

Declaration of competing interest

The authors declare that they have no known competing financial interests or personal relationships that could have appeared to influence the work reported in this paper.

Acknowledgments

The authors are grateful for the financial support from the Science and Technology Program of Xinjiang Uyghur Autonomous Region (No. 2024B01014), the National Science and Technology Major Project of China (No. 2024ZD1404701), and China University of Petroleum (Beijing) Research Start-up Fund (No. 2462025XKBH022).

References

Adrian, V.G., Rached, M.R., Carlos, D.R., et al., 2025. Hydraulic fracture propagation in pre-structured media: Stress field and fracture network topology. Rock Mech. Rock Eng. 59, 3605–3615. https://doi.org/10.1007/s00603-025-05003-8.

Chang, Z., Hou, B., Ding, J.H., 2022. Competitive propagation simulation of multi-clustered fracturing in a cracked shale oil reservoir. Geomech. Geophys. Geo-Energy Geo-Resour. 8, 102. https://doi.org/10.1007/s40948-022-00399-x.

Chen, M., Guo, T.K., Xu, Y., et al., 2022. Evolution mechanism of optical fiber strain induced by multi-fracture growth during fracturing in horizontal wells. Petrol. Explor. Dev. 49 (1), 183–193. https://doi.org/10.11698/PED.2022.01.17.

Chen, R.Z., Zaghloul, M., Yan, A.D., et al., 2016. High resolution monitoring of strain fields in concrete during hydraulic fracturing processes. Opt. Express 24 (4), 3894–3902. https://doi.org/10.1364/OE.24.003894.

Cramer, D., Friehauf, K., Roberts, G., et al., 2020. Integrating distributed acoustic sensing, treatment-pressure analysis, and video-based perforation imaging to evaluate limited-entry-treatment effectiveness. SPE Prod. Oper. 35 (4), 730–755. https://doi.org/10.2118/194334-PA.

Dai, Y.F., Hou, B., Lee, S., et al., 2024. A thermal–hydraulic–mechanical–chemical coupling model for acid fracture propagation based on a phase-field method. Rock Mech. Rock Eng. 57 (7), 4583–4605. https://doi.org/10.1007/s00603-024-03769-x.

Guo, J.C., Zhao, Z.H., Lu, Q.L., et al., 2021. Research progress in key mechanical theories of deep shale network fracturing. Nat. Gas. Ind. 41 (1), 102–117. https://doi.org/10.3787/j.issn:1000-0976.2021.01.009 (in Chinese).

He, J.C., Zhang, K.S., Liu, H.B., 2022. Laboratory investigation on hydraulic fracture propagation in sandstone-mudstone-shale layers. Pet. Sci. 19 (4), 1664–1673. https://doi.org/10.1016/j.petsci.2022.03.018.

Hou, B., Chen, M., Li, Z.M., et al., 2014. Propagation area evaluation of hydraulic fracture networks in shale gas reservoirs. Petrol. Explor. Dev. 41 (6), 763–768. https://doi.org/10.11698/PED.2014.06.18.

Hou, B., Cui, Z., Ding, J.H., et al., 2022a. Perforation optimization of layer-penetration fracturing for commingling gas production in coal measure strata. Pet. Sci. 19 (4), 1718–1734. https://doi.org/10.1016/j.petsci.2022.03.014.

Hou, B., Zhang, Q.X., Liu, X., et al., 2022b. Integration analysis of 3D fractures network reconstruction and frac hits response in shale wells. Energy 260, 124906. https://doi.org/10.1016/j.energy.2022.124906.

Hou, B., Zhang, Q.X., Chen, M., 2023. Status and tendency of physical simulation technology for hydraulic fracturing of shale reservoirs. Petrol. Drill. Techn. 51 (5), 66–77. https://doi.org/10.11911/syztjs.2023096 (in Chinese).

Hou, B., Zhang, Q.X., Lv, J.X., 2024. Distributed fiber optic monitoring of asymmetric fracture swarm propagation in laminated continental shale oil reservoirs. Rock Mech. Rock Eng. 57 (7), 5067–5087. https://doi.org/10.1007/s00603-024-03791-z.

Hu, J.H., Liao, S.Z., Cai, Y.D., et al., 2025. Study of fracture propagation uniformity in deep shale reservoir. Earth Sci. Front. 32 (4), 471–482. https://doi.org/10.13745/j.esf.sf.2024-7-55 (in Chinese).

Jin, G., Ugueto, G., Wojtaszek, M., et al., 2021. Novel near-wellbore fracture diagnosis for unconventional wells using high-resolution distributed strain sensing during production. SPE J. 26 (5), 3255–3264. https://doi.org/10.2118/205394-PA.

Lei, Q., Xu, Y., Cai, B., et al., 2022. Progress and prospects of horizontal well fracturing technology for shale oil and gas reservoirs. Petrol. Explor. Dev. 49 (1), 166–172. https://doi.org/10.11698/PED.2022.01.15.

Li, P.Y., Jin, G., Hammack, R., et al., 2024. Heart shape to fracture distance: Characterizing hydraulic fracture propagation before hits. SPE J. 29 (12), 7122–7133. https://doi.org/10.2118/223631-PA.

Liang, X., Shan, C.A., Zhang, L., et al., 2024. Exploration discovery and accumulation conditions of Da'an deep shale gas field in western Chongqing, Sichuan Basin. Acta Pet. Sin. 45 (3), 477–499. https://doi.org/10.7623/syxb202403001.

Liu, Y.Z., Wu, K., Jin, G., et al., 2020. Rock deformation and strain-rate characterization during hydraulic fracturing treatments: Insights for interpretation of low-frequency distributed acoustic-sensing signals. SPE J. 25 (5), 2251–2264. https://doi.org/10.2118/202482-PA.

Lv, J.X., Hou, B., 2024. Fractures interaction and propagation mechanism of multi-cluster fracturing on laminated shale oil reservoir. Pet. Sci. 21 (4), 2600–2613. https://doi.org/10.1016/j.petsci.2024.02.007.

Ma, W., Wu, K., Jin, G., 2024. Investigation of effective fracture height using strain responses in a vertical monitoring well during a well interference test. SPE J. 29 (9), 4873–4885. https://doi.org/10.2118/217776-PA.

Ma, X.H., Xie, J., 2018. The progress and prospects of shale gas exploration and exploitation in southern Sichuan Basin, NW China. Petrol. Explor. Dev. 45 (1), 161–169. https://doi.org/10.11698/PED.2018.01.18.

Molenaar, M.M., Hill, D.J., Webster, P., et al., 2012. First downhole application of distributed acoustic sensing for hydraulic-fracturing monitoring and diagnostics. SPE Drill. Complet 27 (1), 32–38. https://doi.org/10.2118/140561-PA.

Nolte, D.D., Pyrak-Nolte, L.J., Hopp, C., 2025. Monitoring fracture hydromechanical evolution in the lab and field using unsupervised metric learning. J. Geophys. Res.: Mach. Learn. Comput. 2. https://doi.org/10.1029/2025JH000657 e2025JH000657.

Pakhotina, I., Sakaida, S., Zhu, D., et al., 2020. Diagnosing multistage fracture treatments with distributed fiber-optic sensors. SPE Prod. Oper. 35 (4), 852–864. https://doi.org/10.2118/199723-PA.

Rodriguez, I.V., Wuestefeld, A., 2020. Strain microseismics: Radiation patterns, synthetics, and moment tensor resolvability with distributed acoustic sensing in isotropic media. Geophysics 85 (3), KS101–KS114. https://doi.org/10.1190/GEO2019-0373.1.
Sui, W.B., Wen, C.Y., Sun, W.C., et al., 2023. Joint application of distributed optical fiber sensing technologies for hydraulic fracturing monitoring. Nat. Gas. Ind. 43 (2), 87–103. https://doi.org/10.3787/j.issn.1000-0976.2023.02.009.
Tan, Y.H., Wang, S.G., Rijken, M.C.M., et al., 2021. Geomechanical template for distributed acoustic sensing strain patterns during hydraulic fracturing. SPE J. 26 (2), 627–638. https://doi.org/10.2118/201627-PA.
Tang, X.H., Zhu, H.Y., Che, M.G., et al., 2023. Complex fracture propagation model and plugging timing optimization for temporary plugging fracturing in naturally fractured shale. Petrol. Explor. Dev. 50 (1), 139–151. https://doi.org/10.11698/PED.20221011.
Wang, S., Chen, M., Lv, J.X., 2024. Study of the evolution characteristics of fiber-optic strain induced by the propagation of bedding fractures in hydraulic fracturing. Pet. Sci. 21 (6), 4219–4229. https://doi.org/10.1016/j.petsci.2024.09.010.
Wang, Y.L., Duan, Y.F., Wang, D.B., et al., 2025a. Numerical analysis for center- and edge-type intersections of hydraulic fracture network under varying crossed natural fractures and fluid injection rate. Comput. Part. Mech. 12 (2), 4849–4864. https://doi.org/10.1007/s40571-025-00970-9.
Wang, Y.L., Liu, X.G., Liu, N.N., et al., 2025b. Heterogeneous continuum-discontinuum modeling for dynamic diversion and penetration behaviors of hydraulic fractures contacting multi-layers and granules in tight reservoir rock. Comput. Part. Mech. 12 (2), 4065–4087. https://doi.org/10.1007/s40571-025-01045-5.
Wang, Y.L., Liu, X.G., Liu, N.N., et al., 2025c. Deflection behaviours and fractal morphology of hydraulic fractures meeting beddings and granules with variable geometrical configurations and geomechanical properties. Eng. Comput. 42 (4), 1577–1598. https://doi.org/10.1108/EC-02-2024-0131.
Xie, J.Y., Hou, B., He, M.F., et al., 2024. Fracture-controlled fracturing mechanism and penetration discrimination criteria for thin sand-mud interbedded reservoirs in Sulige gas field, Ordos Basin, China. Petrol. Explor. Dev. 51 (5), 1327–1339. https://doi.org/10.1016/S1876-3804(25)60544-1.
Ye, Z., Ghassemi, A., 2024. Laboratory insights on hydraulic fracture closure and stress measurement. J. Geophys. Res. Solid Earth 130 (7), e2024JB029854. https://doi.org/10.1029/2024JB029854.
Zhang, K., Liu, X.F., Wang, D.B., et al., 2024. A review of reservoir damage during hydraulic fracturing of deep and ultra-deep reservoirs. Pet. Sci. 21 (1), 384–409. https://doi.org/10.1016/j.petsci.2023.11.017.
Zou, C.N., Zhao, Q., Cong, L.Z., et al., 2021. Development progress, potential and prospect of shale gas in China. Nat. Gas. Ind. 41 (1), 1–14 https://doi.org/10.3787/j-issn:1000-0976-2021.01.001 (in Chinese).